NANO LETTERS

Letter

pubs.acs.org/NanoLett

Highly Scalable, Uniform, and Sensitive Biosensors Based on Top-Down Indium Oxide Nanoribbons and Electronic Enzyme-Linked Immunosorbent Assay

Noppadol Aroonyadet,[†,¶] Xiaoli Wang,[†,¶] Yan Song,[‡,¶] Haitian Chen,[†] Richard J. Cote,[§]
Mark E. Thompson,[‡] Ram H. Datar,[*,§] and Chongwu Zhou[*,†]

[†]Department of Electrical Engineering, [‡]Department of Chemistry, University of Southern California, Los Angeles, California 90089, United States

[§]Department of Pathology, University of Miami, Miami, Florida 33136, United States

Ⓢ *Supporting Information*

ABSTRACT: Nanostructure field-effect transistor (FET) biosensors have shown great promise for ultra sensitive biomolecular detection. Top-down assembly of these sensors increases scalability and device uniformity but faces fabrication challenges in achieving the small dimensions needed for sensitivity. We report top-down fabricated indium oxide (In_2O_3) nanoribbon FET biosensors using highly scalable radio frequency (RF) sputtering to create uniform channel thicknesses ranging from 50 to 10 nm. We combine this scalable sensing platform with amplification from electronic enzyme-linked immunosorbent assay (ELISA) to achieve high sensitivity to target analytes such as streptavidin and human immunodeficiency virus type 1 (HIV-1) p24 proteins. Our approach circumvents Debye screening in ionic solutions and detects p24 protein at 20 fg/mL (about 250 viruses/mL or about 3 orders of magnitude lower than commercial ELISA) with a 35% conduction change in human serum. The In_2O_3 nanoribbon biosensors have 100% device yield and use a simple 2 mask photolithography process. The electrical properties of 50 In_2O_3 nanoribbon FETs showed good uniformity in on-state current, on/off current ratio, mobility, and threshold voltage. In addition, the sensors show excellent pH sensitivity over a broad range (pH 4 to 9) as well as over the physiological-related pH range (pH 6.8 to 8.2). With the demonstrated sensitivity, scalability, and uniformity, the In_2O_3 nanoribbon sensor platform makes great progress toward clinical testing, such as for early diagnosis of acquired immunodeficiency syndrome (AIDS).

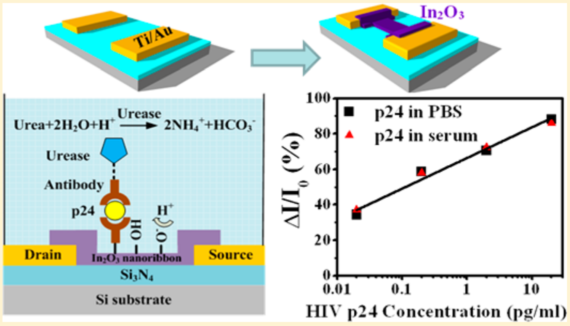

KEYWORDS: *nanoribbon, indium oxide, biosensor, electronic ELISA, top-down fabrication*

Nanobiosensors based on nanostructure field-effect-transistors (FETs) have become an area of intense research because their detection of biomolecules has potential applications ranging from health monitoring to drug discovery. Their real-time, highly sensitive, and electrical sensing capabilities have been demonstrated in the detection of biomolecules such as proteins,[1−5] nucleic acids,[6,7] viruses,[8] and other small molecules.[9] Nanobiosensors fabricated using bottom-up assembly, such as nanowire biosensors, are highly sensitive because bottom-up synthesis yields high crystalline quality and critical dimensions as small as a few nanometers.[1,10] Top-down biosensors, on the other hand, can add scalability and device uniformity, but must overcome fabrication challenges to achieve similar sensing performance. This has propelled the recent emergence of several top-down nanobiosensor fabrication techniques based on silicon-on-insulator (SOI) and polysilicon materials.[2,11−13] Among these, electron-beam lithography,[14] imprint lithography,[15] spacer technique,[12] and photolithography[2] have been explored to optimize dimensional control and scalability with promising results. Specifically, top-down nanoribbon biosensors, with relaxed lateral dimensions, have allowed straightforward photolithographic processing, resulting in high uniformity and functional device yield. This relaxed dimensional requirement can be achieved without losing sufficient sensitivity because the critical dimension, which is the channel depth, remains in the nanoscale. Their larger area also provides more surface for analytes to bind.[11,16]

Metal oxides have been traditionally used as sensor materials because their surfaces are very sensitive to changes in the environment.[17−19] Metal oxides are inherently semiconducting without impurity doping, and their electrical properties are stable during sensing. As an example, In_2O_3 nanowires have been successfully applied to highly sensitive chemical sensors,[18,20] biosensors,[3−5] optical detectors,[21] thin film transistors (TFTs),[22] and other electronic applications.[23] In

Received: December 13, 2014
Revised: January 23, 2015

DOI: 10.1021/nl5047889
Nano Lett. XXXX, XXX, XXX−XXX

this work, we investigate the sensing properties of In_2O_3 nanoribbon FET biosensors for the detection of human immunodeficiency virus type 1 (HIV-1) p24 antigen. The In_2O_3 nanoribbon thickness is well controlled by the highly scalable radio frequency (RF) sputtering technique, and the entire sensor is fabricated by a top-down, two-mask conventional photolithography process.

Diagnosis of HIV-1 infection, the cause of acquired immune deficiency syndrome (AIDS), relies on the detection of HIV-1 ribonucleic acid (RNA), capsid antigen p24, and anti-HIV antibody.[24] Most common food and drug administration (FDA)-approved HIV-1 diagnostic assays target HIV-1 RNA because of the ease of polymerase chain reaction (PCR) mediated amplification. Although this method is very sensitive, it is expensive, requires well-trained staff, and must be performed in well-equipped laboratories. RNA testing in rural or remote settings is also a major challenge. Testing for the HIV-1 p24 antigen is a good alternative because it can be done in resource-limited situations. Antigen p24 level is significantly high during the early, acute phase of infection and the terminal stage of AIDS. It is also a useful marker for predicting CD4+ T cell count decreases, disease progression for early detection of HIV-1 infection, and patient prognosis. Early detection of HIV infection helps to prevent HIV transmission and to prolong AIDS condition by receiving proper treatment. HIV-1 p24 antigen is usually detected by enzyme-linked immunosorbent assay (ELISA). However, the detection sensitivity of the conventional assay is less than desirable: 10−20 pg/mL.[25,26] Many research groups have tried to lower the limit of detection for early diagnosis of HIV using several approaches such as modifying ELISA with a booster step,[25] sandwich p24 amperometric immunosensor based on a modified electrode,[27] nanoparticle based fluorescent assay[26,28] and atomic force microscopy of sandwich HIV p24 nanoarrays[29] to the level close to HIV nucleic acid amplification test.[30,31] From these attempts, the lowest detectable level of HIV p24 based on modified ELISA techniques is 10 fg/mL with the projected limit of detection to be 5 fg/mL.[28] As an alternative approach, we demonstrate In_2O_3 nanoribbon biosensors detection of p24 proteins at 20 fg/mL, or about 250 viruses/mL,[28] with a 35% conduction change from a baseline conduction measured in human blood serum. We have projected limit of detection of our sensors to be about 200 ag/mL with 1% change in conduction. This detection limit can possibly diagnose HIV infection about 7 to 10 days earlier than the detectable window enabled by conventional ELISA.[28] In fact, this detection limit is much closer to the 40 HIV viruses/mL detection limit from PCR.[30,31] We are able to achieve this sensitive electrical detection in physiological solutions because electronic ELISA circumvents Debye length screening of electrical signals in high salt concentration and has amplification from the enzyme−substrate reaction. Moreover, the scalable and low-cost nanoribbon platform can be highly portable for point-of-care field testing.

The fabrication of In_2O_3 nanoribbon biosensors requires two photolithography steps. First, 500 nm of Si_3N_4 is deposited on Si substrates by low pressure chemical vapor deposition (LPCVD). Silicon nitride is used instead of silicon dioxide as the passivation layer because it is more resistant to our surface chemistry, resulting in better suppression of competition binding of biomolecules to the surface of the substrate. In Figure 1a, the first lithography step defines the source and drain electrodes. It is followed by electron beam evaporation of 5 nm Ti and 45 nm Au, as shown in Figure 1b. After that, both the dimension and the position of the nanoribbons are defined by the second mask, as shown in Figure 1c. The In_2O_3 nanoribbons are then deposited by RF sputtering with thickness targeted at 10 to 50 nm. Nanoribbons are formed after the lift-off process, which is the last step in the fabrication. Because nanoribbons are never exposed to any additional layer or photoresist, this fabrication order leaves a pristine nanoribbon surface for surface chemistry. Figure 1d shows a wafer-scale photo of the fabricated In_2O_3 nanoribbon FETs with 100% yield, and its inset shows a magnified optical image of one nanoribbon chip, which contains four subgroups of six nanoribbon FET devices. A comparison between the scanning electron microscopy (SEM) images of two nanoribbon FETs in Figure 1f shows that the 50 μm by 2 μm channels are identical. This uniformity in fabrication is expected to extend to the electrical properties of the devices.

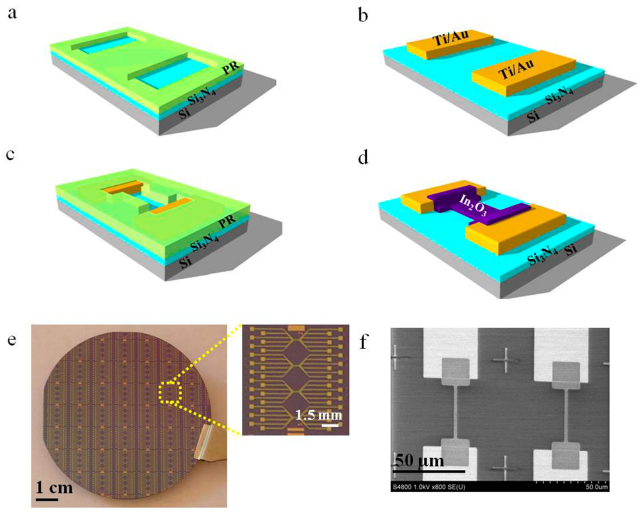

Figure 1. Fabrication processes of In_2O_3 nanoribbon biosensors. (a) First photolithography step defining metal electrodes on top of Si_3N_4 on Si wafer substrate, (b) 5/45 nm Ti/Au metal electrode deposited by evaporation followed by lift-off. (c) The second photolithography step defining nanoribbon active channel. (d) In_2O_3 was deposited by RF sputtering and lift-off to expose In_2O_3 nanoribbon channel. (e) Optical image of a 3 in. wafer of In_2O_3 nanoribbon biosensors. Inset shows a magnified image of a nanoribbon chip composing of four subgroups of six nanoribbon devices. (f) SEM micrograph of nanoribbon devices in a subgroup.

After device fabrication, In_2O_3 nanoribbon FETs were characterized by an Agilent semiconductor analyzer 4156B using a back gate. Figure 2a and b, respectively, show family plots of drain current−drain voltage ($I_{DS}-V_{DS}$) and drain current−gate voltage ($I_{DS}-V_{GS)}$) curves measured from an In_2O_3 nanoribbon device. Figure 2a exemplifies a good metal oxide semiconductor field effect transistor (MOSFET) behavior where I_{DS} varies linearly with V_{DS} at low voltage range and saturates at voltages higher than 20 V. In addition, both Figures 2a and 2b show that I_{DS} decreases with decreasing $V_{GS,}$ in accordance with n-channel transistor behavior. From both the $I_{DS}-V_{DS}$ and the $I_{DS}-V_{GS}$ plots, the device is turned off at V_{GS} below 0 V, with on/off current ratios in the range of 10^5 to 10^6.

Besides In_2O_3, we have also studied other possible materials using this top-down approach. In Figure S2a−f in the Supporting Information, we have included family $I_{DS}-V_{DS}$ and $I_{DS}-V_{GS}$ plots for sputtered InGaZnO, SnO_2, and ITO nanoribbon devices. Both InGaZnO (Supporting Information

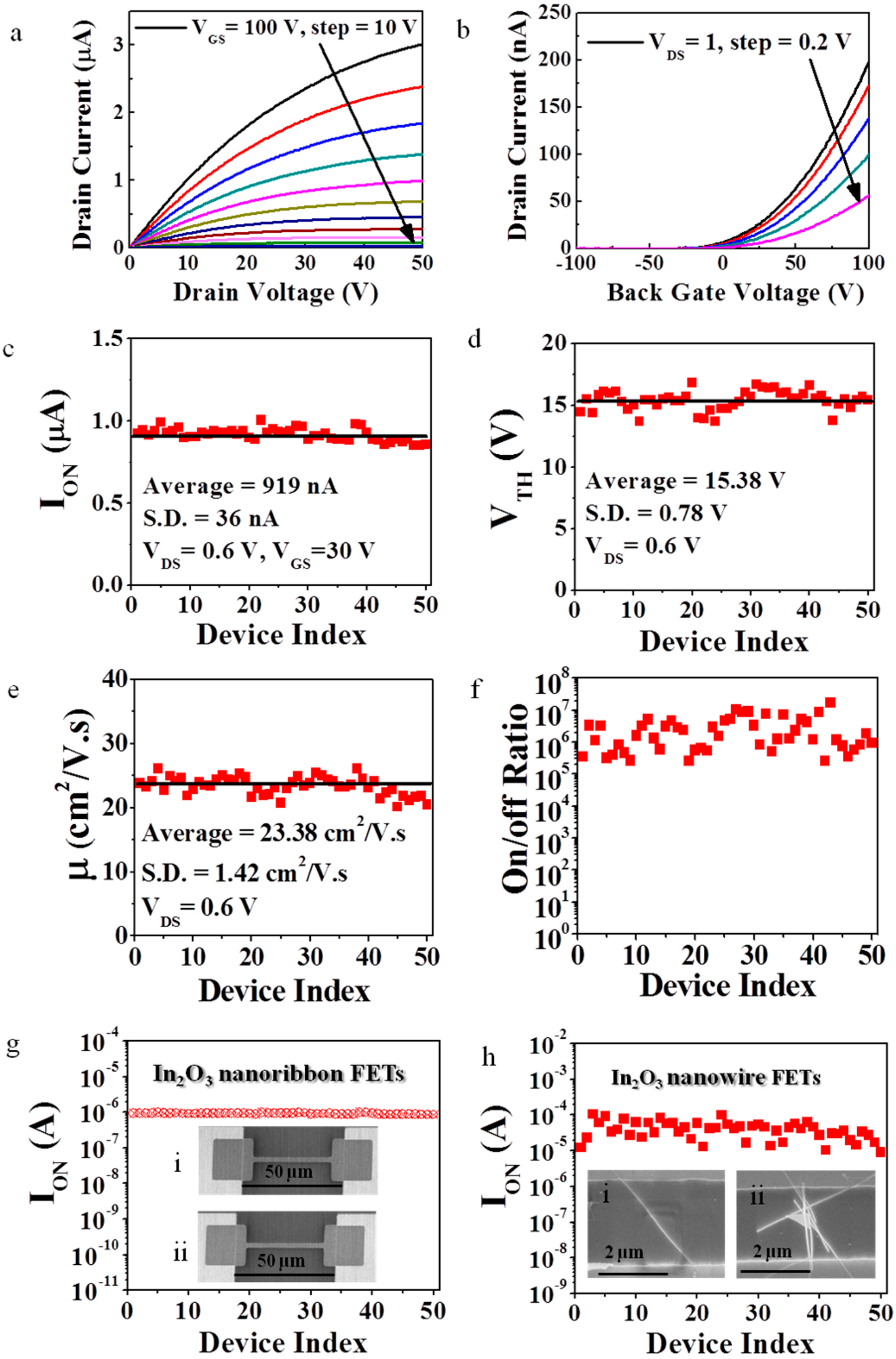

Figure 2. (a) Family of I_{DS}−V_{DS} curves and (b) a family of I_{DS}−V_{GS} curves from an In_2O_3 nanoribbon FET. Plots of electrical performance from 50 In_2O_3 nanoribbon transistors (c) On-state current (I_{ON}) at V_{GS} = 30 V and V_{DS} = 600 mV. (d) Threshold voltage (V_{TH}) (e) Mobilities (μ) and (f) On/off current ratios at V_{DS} = 600 mV. (g) On-state current measured from 50 In_2O_3 nanoribbon devices from (c) in logarithmic scale with two identical SEM inset images taken from different representative devices on the substrate. (h) On-state current measured from 50 devices In_2O_3 nanowire FET devices with inset SEM images taken from two different devices to show nonuniformity of nanowire devices.

DOI: 10.1021/nl5047889
Nano Lett. XXXX, XXX, XXX−XXX

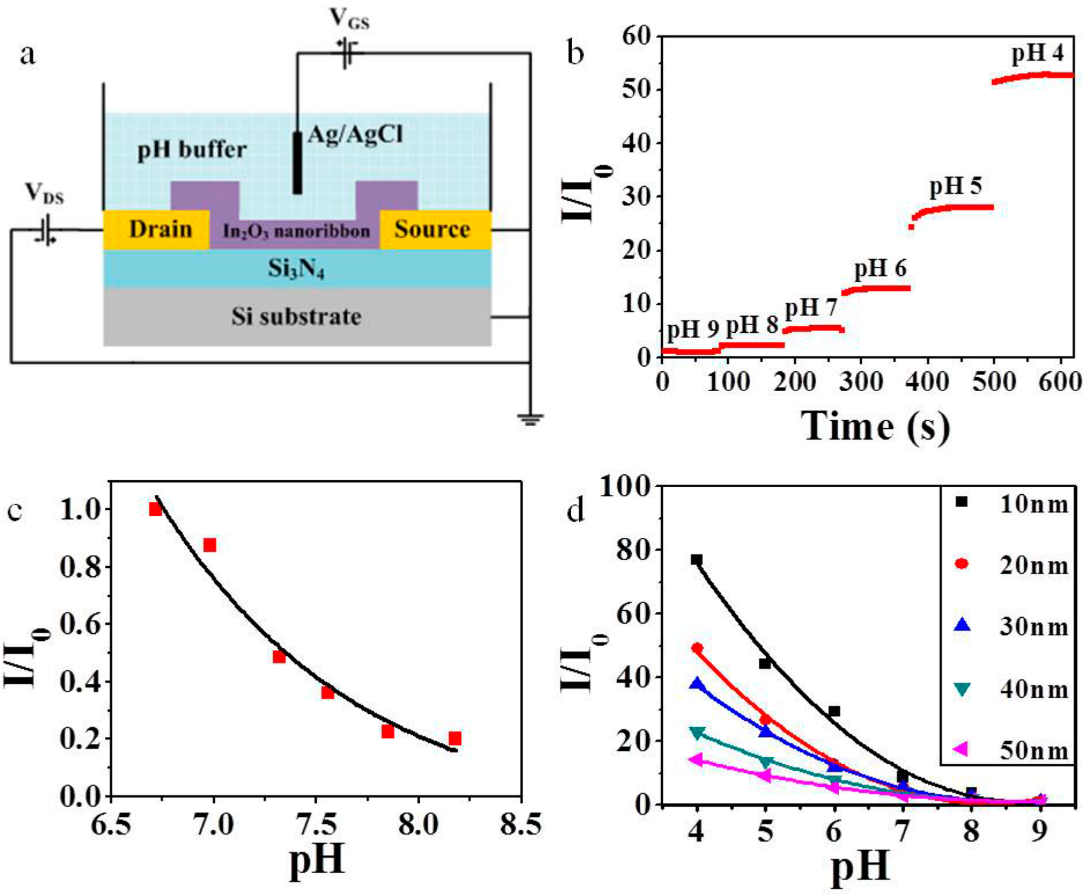

Figure 3. (a) Schematic diagram of pH sensing experiment on In_2O_3 nanoribbon devices. Commercial pH buffer solution was confined in a Teflon electrochemical chamber. Liquid gate voltage was applied through a Ag/AgCl electrode. (b) Real-time responses obtained from a 20 nm In_2O_3 nanoribbon device exposed to commercial buffer solutions with pH 4 to 9 (c) Real-time responses obtained from three 20 nm In_2O_3 nanoribbon devices in buffer solutions with pH in the physiological range 6.7 to 8.2 with step of 0.3. (d) Real-time responses from In_2O_3 nanoribbon devices at different thickness ranging from 10 to 50 nm exposed to commercial buffer solutions with pH 4 to 9.

Figures S2a and b) and SnO_2 (Supporting Information Figure S2c and d) show good MOSFET behavior, but they are 10 and 100 times more resistive than the In_2O_3 nanoribbon device, respectively. Furthermore, SnO_2 and InGaZnO nanoribbon devices have threshold voltages (V_{TH}) between 50 to 60 V and on/off current ratios in the range of 10^3 to 10^5, making these two materials less efficient and less sensitive than In_2O_3 as FET sensors. Measurements of ITO nanoribbon devices (Figures S2e and f in the Supporting Information) show even less desirable MOSFET behavior. They exhibit poor gate voltage dependence and a low on/off current ratio around one. Another metal oxide commonly used for transistors and sensors, ZnO, also proves to be incompatible with biosensing in a liquid environment. Figure S2g and h in the Supporting Information show optical images of as-fabricated ZnO nanoribbons in air and after 14 h in 1× phosphate buffer saline (PBS), respectively. We observed that ZnO is unstable in the PBS solution and dissolved completely after 14 h. These results support In_2O_3 as the optimal nanoribbon material for our study.

Statistical analyses of key electrical properties for 50 In_2O_3 nanoribbon FETs are plotted in Figure 2c to f. The dielectric used in these studies is 50 nm SiO_2. The average on-state current (I_{ON}) measured at V_{DS} = 600 mV and V_{GS} = 30 V is 918.6 nA with a standard deviation of 36 nA, or 4% from the average value, as shown in Figure 2c. The V_{TH} is extracted from the $I_{DS}-V_{GS}$ curve with V_{DS} set to 600 mV, and the distribution is plotted in Figure 2d with an average of 15.38 V and a standard deviation of 0.78 V, or 5% of the average. The electron mobility (μ) was calculated from the relationship $g_m = \mu(C/L^2)$ V_{DS} where g_m is taken as the maximum of the derivative of the $I_{DS}-V_{GS}$ curve. The gate capacitance (C) was calculated from the parallel plate model ($C = \varepsilon A/d$), and the channel length (L) is 80 μm. With a SiO_2 relative dielectric constant of 3.9, calculated plate area (A) of 460 μm^2, and SiO_2 dielectric thickness (d) of 50 nm, the gate capacitance is calculated to be 3.18×10^{-13} F. From these parameters, mobilities of all 50 devices are calculated and plotted in Figure 2e. The average electron mobility is 23.38 $cm^2/(V{\cdot}s)$, and the standard deviation is 1.42 $cm^2/(V{\cdot}s)$ or 6% of the average. Lastly, Figure 2f shows the on/off current ratios from 50 devices. Most of the In_2O_3 nanoribbon devices demonstrate a good on/off ratio between 10^5 to 10^7. To bench mark the uniformity of our "top-down" nanoribbon devices, the I_{ON} of 50 In_2O_3 nanoribbon FETs (Figure 2g) is compared to that of 50 In_2O_3 nanowire FETs shown in Figure 2h. In_2O_3 nanoribbon devices show more uniform on-state current than nanowire devices due to their high dimensional control. The SEM insets in Figure 2g of two identical representative devices reflect the low device-to-device variation of the "top-down" approach. On the other hand, the large variation in the on-state current of In_2O_3 nanowire devices are attributed to the difference in the number of nanowires bridging between metal electrodes, as shown in the inset SEM images in Figure 2h. This variation is inherent in the "bottom-up" fabrication process.

In addition to demonstrating the electrical uniformity of In_2O_3 nanoribbon devices in air, we have also measured 30 devices in 0.01× PBS buffer solution to investigate sensor uniformity in the biosensing environment. Key characteristics in solution are shown in Figure S3 in the Supporting Information. Supporting Information Figure S3a shows that the average of the I_{ON} measured at V_{DS} = 200 mV and liquid gate voltage (V_{LG}) = 1 V is 1.39 μA, with a standard deviation of 0.11 μA (8% of the average). Transconductance (g_m) of these 30 devices (Supporting Information Figure S3b) falls in a narrow distribution between 3.5 to 4.5 μS, with the average at 3.76 μS and a standard variation of 0.30 μS (8% of average). Supporting Information Figure S3c shows that variation in V_{TH} is also small, with the average at 0.53 V and the standard variation at 0.01 V, only 2% of the average. Lastly, on/off current ratios fall between 10^4 and 10^5 (Supporting Information Figure S3d). The small device-to-device variations in liquid environment show good potential for biosensing.

For biosensing applications, devices are regularly exposed to fluids with certain ionic concentration and osmolarity. The time of exposure can even be lengthened for monitoring cellular signals from live cells. The electrical stability of devices in such media will play an important role toward biosensing applications because degraded devices can give false signals. To test device stability in physiological fluids, we immerse the devices in 1xPBS as the model fluid. Electrical measurements were taken once every 10 days for the first 50 days, then once every 30 days after the initial 50 day period. Key electrical characteristics of 18 In_2O_3 nanoribbon sensors were extracted from their $I_{DS}-V_{LG}$ curves and plotted in Figure S5 in the Supporting Information. In Supporting Information Figure S5a, the average I_{ON} retained about 70% of the initial average current after 80 days and remained stable around this level after 4 months. In Supporting Information Figure S5b and c, fluctuations in both the average g_m and V_{TH} are within around 30% of the initial values. In Supporting Information Figure S5d, the median on/off current ratio remained within an order of magnitude after 4 months. These trends show good long-term stability of the In_2O_3 nanoribbon sensors in physiological fluids, and this is achieved without requiring additional protection layers to prevent the hydrolysis of native oxide as in the case of silicon channels.[32] This advantage makes the In_2O_3 nanoribbon platform a promising candidate for in vivo and in vitro applications.

To test the sensitive of the In_2O_3 nanoribbon FET biosensors to changes in ionic concentration, we conducted a series of pH detection experiments under different conditions, as shown in Figure 3. A schematic diagram of the setup for pH sensing is shown in Figure 3a. We mechanically mount a Teflon electrochemical cell on top of an In_2O_3 nanoribbon chip in order to confine the sensing solution to the FET channel area. Then we manually exchange different solutions varying in pH in and out of the sensing chamber using pipettes. Figure 3b shows the real-time sensing response of a 20 nm unfunctionalized In_2O_3 nanoribbon device to commercial pH buffer solutions ranging from pH 4 to pH 9. The device shows an increase in conduction with decreased pH. This trend agrees with the gate voltage modulation behavior of n-channel transistors: a higher number of positive hydrogen ions in a lower pH solution yields higher current due to a positive gating effect on the In_2O_3 nanoribbon device. The normalized sensing response shows excellent pH sensitivity over a wide range between pH 4 to 9. To test the nanoribbon device sensitivity to pH changes in a range more relevant for biosensing applications, we have performed pH sensing experiment in the physiological range from pH 6.7 to pH 8.2, with steps of about 0.3. Figure 3c shows the average of the normalized current responses from three In_2O_3 nanoribbon FETs with 20 nm thickness. These devices show a 5 times decrease in conduction with a pH change of 1.5.

We have also investigated the dependence of sensor performance on the nanoribbon depth by comparing pH sensing signals from sensors with varying thicknesses. The distance into the semiconducting nanoribbon at which surface charges are no longer felt is defined as the Debye length, $\lambda_D = (\epsilon k_B T/(q^2 n))^{1/2}$, where ϵ, k_B, T, q, and n stand for the permittivity (7.97×10^{-13} F/cm for In_2O_3),[33] the Boltzmann's constant, temperature, charge constant, and charge density, respectively.[11] To achieve good sensitivity, the optimal nanoribbon thickness needs to be within the transistor Debye length. For the In_2O_3 nanoribbons, this Debye length is calculated to be 23 nm using methods described in the Supporting Information. To test how this affects pH sensitivity, In_2O_3 nanoribbons are fabricated with thicknesses ranging from 10 to 50 nm. As shown in Figure 3d, conduction of all devices decreases exponentially when the pH increases from pH 4 to 9, regardless of the nanoribbon depth. Similar exponential conduction change in response to pH variation has been observed from the unfunctionalized Si nanowire FET platform.[1] As expected, the 10 and 20 nm In_2O_3 nanoribbon devices are the most sensitive to the ionic change in the buffer solution because it is easier to deplete carriers in the channel with thickness within the Debye length. However, the 10 nm In_2O_3 nanoribbon FET also shows the highest fluctuation in sensing signals, which can be contributed to lower film uniformity during In_2O_3 deposition. For the rest of the experiment, we targeted a 20 nm ribbon thickness, which gives us good stability and sensitivity.

To study the dependence of In_2O_3 nanoribbon sensitivity on crystallinity, we annealed 20 nm In_2O_3 films and nanoribbon devices at 300 °C for 30 min in low vacuum condition to obtain polycrystalline In_2O_3. Figure S4a and b in the Supporting Information show X-ray diffraction (XRD) patterns of as-sputtered and annealed In_2O_3 films, respectively. In Supporting Information Figure S4a, no In_2O_3 peaks were observed from the as-sputtered film, which confirms the amorphous nature of as-sputtered In_2O_3 nanoribbons. In contrast, the XRD pattern of the annealed In_2O_3 film in Supporting Information Figure S4b shows peaks for the (222), (400), (440), and (622) In_2O_3 planes. These multiple peaks are indicators of polycrystallinity and were also observed by other researchers.[34] Next, we performed a pH sensing experiment to compare the results from both the polycrystalline and the amorphous In_2O_3 nanoribbon devices. Figure S4c in the Supporting Information shows average pH sensing responses from three devices of annealed and nonannealed In_2O_3 nanoribbon FETs. Both types of devices showed comparable performance in detecting pH from 4 to 9. From this demonstration, we believe it is unnecessary to perform additional postannealing to obtain polycrystalline structure for sensing.

After confirming strong sensitivity of In_2O_3 nanoribbon devices to charges in fluids, we applied a phosphonic acid functional group as the linker molecule to covalently anchor

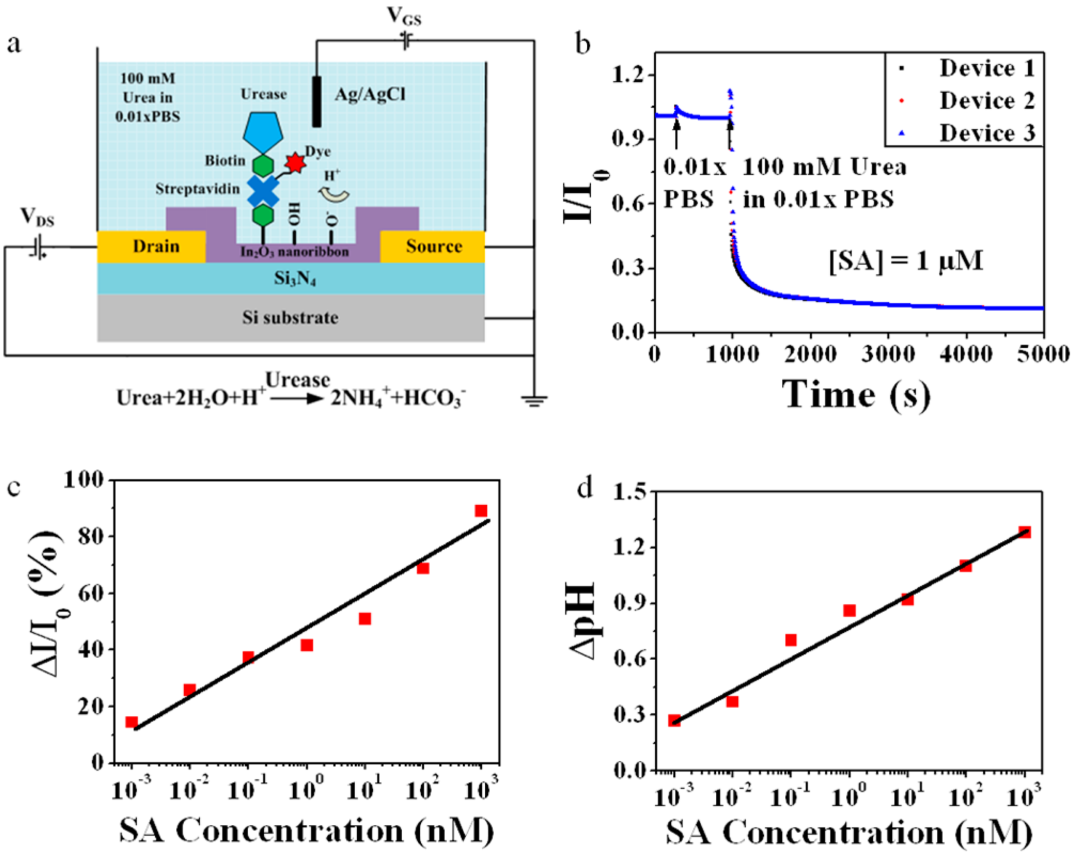

Figure 4. (a) Schematic diagram of streptavidin electronic ELISA. (b) Normalized real-time responses of 1 μM streptavidin electronic ELISA from three In_2O_3 nanoribbon devices monitored simultaneously. Introducing urea into the sensing chamber, hydroxyl groups on the surface of nanoribbon are deprotonated due to urea−urease enzyme reaction that consumes hydrogen ions in the solution yielding more negatively gating effect and decrease in electrical conduction of nanoribbon devices. (c) Plot of average normalized current responses and streptavidin concentration calculated from three devices monitored simultaneously in each concentration. (d) Plot of pH changes in the sensing chamber measured by a commercial pH meter and streptavidin concentration.

probe biomolecules to the In_2O_3 surface for specific sensing. The same phosphonic acid to In_2O_3 chemistry, along with the *N*-(3-(dimethylamino)propyl)-*N*′-ethylcarbodiimide hydrochloride (EDC)/*N*-hydroxysuccinimide (NHS) coupling to biomolecules, has been demonstrated in previous studies on In_2O_3 nanowire-based devices.[3,5] Details of the surface chemistry and fluorescence confirmation of the phosphonic acid functionalization can be found in the Supporting Information. Supporting Information Figure S6a and b show schematic diagrams of how fluorescent experiments were performed using biotin and fluorescent dye-tagged streptavidin as the model probe-analyte system. The negative controls are anchored with amine poly(ethylene glycol) (PEG) as the probe instead of biotin. Supporting Information Figure S6c and d show the substrate schematic diagram and its optical image, respectively. Supporting Information Figure S6e−h show that In_2O_3 ribbons with biotin probes are bright while the ribbons with amine PEG probes are dark, confirming successful binding of probe biomolecules using the phosphonic acid chemistry. These four experiments also show that the phosphonic acid chemistry will react with the SiO_2 substrate, whereas the Si_3N_4 substrate can be used to suppress such competition binding if necessary.

Direct electrical detection of biomolecules in their physiological environment is often impeded by Debye screening from the high salt concentration in the sample solution. Sandwich ELISA,[35] on the other hand, detects signals associated with the reactions between the substrate solution and the conjugated enzymes on secondary antibodies instead of the biomarker. The sandwich structure not only overcomes the Debye screening issue but also incorporates an amplification scheme to lower the signal-to-noise ratio (SNR), which can be much higher for direct analyte detection without amplification, especially when the amount of analytes are small. In the following In_2O_3 nanoribbon sensing experiments, we applied an electronic ELISA technique that uses pH change due to urease enzyme activity as the amplification signal. The urease enzymes are linked to the secondary antibody through biotin and streptavidin. When a solution of urea is introduced to nanoribbon sensor surface with the sandwich structure, the urea causes an increase in the pH of the solution due to consumption of hydrogen ions according to the reaction[36]

$$\text{Urea} + 2H_2O + H^+ \xrightarrow{\text{Urease}} 2NH_4^+ + HCO_3^-$$

The urease deprotonates free hydroxyl groups on the surface of In_2O_3 nanoribbon, and the pH increases due to the reduction of positive hydrogen ions and surface potential. The increase in negative surface charges is responsible for the decrease in conduction of the n-type In_2O_3 nanoribbon FETs. The pH change is easily measured by the In_2O_3 nanoribbon sensors because more charges are released during the pH increase than from the direct binding between an analyte and a probe antibody. This allows the sensor to detect very low

DOI: 10.1021/nl5047889
Nano Lett. XXXX, XXX, XXX−XXX

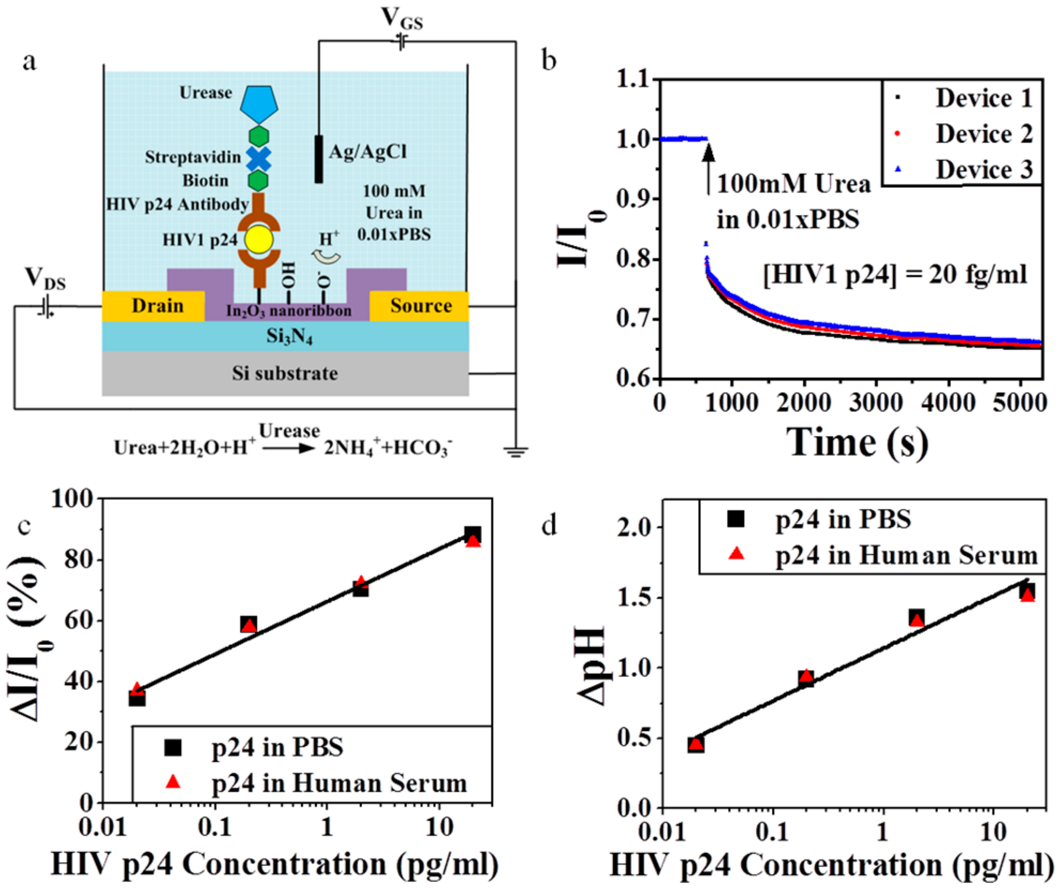

Figure 5. (a) Schematic diagram of electronic ELISA for HIV1 p24 detection. (b) Real-time responses monitored from 3 In_2O_3 nanoribbon devices simultaneously at 20 fg/mL of p24 proteins in PBS. Conduction of all devices decreased upon presence of urea in the sensing chamber. (c) Plot of average normalized responses from 3 devices at each p24 concentration and p24 concentration in picograms per milliliter. (d) Plot of change in pH in the sensing chamber measured from a commercial pH meter and p24 protein concentration in picograms per milliliter.

concentrations of the analyte in physiological samples without the limitation of the Debye screening effect.[36]

We performed electronic ELISA sensing on streptavidin first so that the electrical signal can be confirmed by the fluorescence signal from the binding between biotin and streptavidin tagged with fluorescent dye. Figure 4a shows a schematic diagram of the sensing setup and the sequence of molecule binding. Cleaned In_2O_3 nanoribbon devices were functionalized with 1 mM biotinylated phosphonic acid linkers (details of biotinylated phosphonic linker synthesis and surface functionalization are described in the Supporting Information) in methanol for 5.5 h. Devices were then immersed in a solution of streptavidin conjugated with red fluorescent dye for 2 h at room temperature before rinsing off excess streptavidin. Fluorescence confirmation of streptavidin binding is shown in Figure S7 in the Supporting Information. In Supporting Information Figure S7a, the optical photograph shows one In_2O_3 nanoribbon device after incubating in 1 μM of dye-tagged streptavidin. Supporting Information Figure S7b shows the fluorescence image taken from the same device in Supporting Information Figure S7a. The strong fluorescence on the In_2O_3 suggests that binding between biotin and streptavidin has occurred.

After attaching streptavidin, the devices were incubated in 100 μg/mL biotinylated urease enzymes in 1xPBS for 2 h at room temperature before rinsing off any excess protein. The amount of urease enzymes was determined by streptavidin concentration anchored on the nanoribbon surface. To perform the sensing, we immersed the devices in a baseline solution of 0.01× PBS with pH 7.4. This was then replaced with 100 mM urea in 0.01× PBS (pH = 6.61) to detect the presence of streptavidin. Figure 4b shows the real-time responses when the urea solution was introduced into the sensing chamber. The urease-urea interaction drastically reduced the device to 11.2% of the baseline signal. The pH of the final solution in the sensing chamber was measured to be 8.68 by a commercial Mettler Toledo pH meter. The 1.28 increase in pH is consistent with the decrease in conduction of the In_2O_3 nanoribbon device. Furthermore, a control experiment has been performed by introducing 100 mM of the urea solution to the chamber before the incubation of biotinylated urease. The pH of the final solution of the control experiment is the pH of the 100 mM urea (6.61). This decrease in pH from the baseline increased the sensor conduction, as shown in Figure S7c in the Supporting Information, further suggesting that the conduction decrease in Figure 4b is indeed due to urea interaction with the urease enzyme that is part of the sandwich system containing the target biomarker.

To ensure that the sensing response is generated from the In_2O_3 nanoribbon device instead of the surrounding fluids, we performed experiments to measure the electrical current from a device with an In_2O_3 nanoribbon and a device without any In_2O_3 nanoribbon immersed in 0.01× PBS as shown in Figure S8 in the Supporting Information. Supporting Information

Figure S8a shows plots of $I_{DS}-V_{LG}$ from devices with and without In_2O_3 nanoribbon. We found that the In_2O_3 nanoribbon device exhibits good gate dependence with I_{DS} about 1.3 μA at V_{LG} = 1 V and V_{DS} = 200 mV. The device without any nanoribbon bridging between source and drain electrodes does not show any gate dependence and its electrical current is negligible. Supporting Information Figure S8b and c show sampling responses of devices with and without In_2O_3 nanoribbon. We observed about 320 nA from an In_2O_3 nanoribbon device and about 4.5 pA from the device having only electrodes without any In_2O_3 nanoribbon, or about 5 orders of magnitude different in conduction between these two devices. From these experiments, we can conclude that device conduction is generated from In_2O_3 nanoribbon biosensors and not contributed from conduction between source and drain metal electrodes via the buffer solution.

After testing with 1 μM streptavidin concentration, we repeated real-time sensing for other streptavidin concentrations, namely 100 nM, 10 nM, 1 nM, 100 pM, 10 pM, and 1 pM. Figure 4c shows normalized steady state responses for each of the above streptavidin concentrations. Each data point is an average of three sensors. The response increases exponentially with increasing streptavidin concentration. The change in pH between the final urea solution in the sensing chamber and baseline 0.01× PBS buffer is plotted against streptavidin concentration as shown in Figure 4d. This relationship also shows the same exponential trend. With the pH amplification scheme enabled by the electronic ELISA, our nanoribbon biosensors have detected a streptavidin concentration that is 4 orders of magnitude lower than the 1 nM reported for In_2O_3 nanowire sensors with the same magnitude of the sensing response (about 2%).[5]

The ultra low limit of detection demonstrated by our nanoribbon platform is advantageous for detecting biomarkers like the HIV p24 protein, whose presence even at an extreme low level can indicate early stage of HIV infection. To perform electronic ELISA detection for the p24 protein, we functionalized our devices with the phosphonic linker molecules and used EDC/NHS chemistry to anchor the HIV1 p24 antibodies on the surface of nanoribbons, as mentioned in the Method Section. Known concentrations of the p24 proteins in 1× PBS buffer were then introduced to the sensor for antigen−antibody binding. Next, the secondary biotinylated HIV1-p24 antibodies were anchored on the captured proteins by incubation at room temperature for 4 h before rinsing extensively with 1× PBS. After that, devices were incubated in 100 pM streptavidin in 1× PBS to provide binding sites for 0.1 mg/mL biotinylated urease enzymes, which is the last step before the sensing. Urease enzymes can also be directly linked to the secondary antibody to reduce the number of binding steps. Figure 5a shows the schematic diagram for the above sequence of molecules in the electronic ELISA for p24 protein detection.

Figure 5b shows normalized real-time electronic-ELISA sensing responses to HIV1 p24 at 20 fg/mL monitored from three In_2O_3 nanoribbon devices simultaneously. The conduction of the devices was reduced by about 35% when they were exposed to 100 mM urea solution because of the increase in the pH of solution in the sensing chamber that was induced by reaction between immobilized urease enzymes and urea solution. Figure 5c shows a plot of average normalized responses from three devices monitored simultaneously at each different p24 protein concentration from 20 fg/mL to 20 pg/mL. Responses from electronic-ELISA show exponential relation with p24 concentration as shown in Figure 5c. Figure 5d shows a plot of pH changes in the sensing chamber before and after sensing measured by a pH meter and p24 concentration. It also shows an exponential relationship, which agrees with the trend of changes in conduction in Figure 5c.

In addition, we have spiked known concentrations of p24 proteins in human serum as the target analytes in several electronic ELISA experiments in order to demonstrate the capability of our devices to selectively perform sensing in the physiological solutions. We observed similar changes in electrical conduction and in the pH of the sensing solution to what we had obtained from p24 sensing in PBS, despite the fact that blood serum is composed of numerous competing proteins such as human serum albumins and human serum globulins.[37] The PBS sensing data are shown as black rectangles, and human serum data are shown as red triangles in Figure 5c and d, respectively. The matching of the buffer and the serum data is a good indicator that the signals from both media are attributed to mainly the p24 proteins and not the competing proteins in the physiological fluid. These results serve as a good evidence for the selectivity of our sensors in the complex media because our devices can selectively detect p24 proteins in human serum. As a result, we can use this electronic ELISA approach in different kinds of physiological solutions without complicated sample preparation steps, as competing proteins/biomolecules in the fluids are washed off, leaving only target analytes immobilized by capture probes. From our approach, we could detect HIV-1 p24 proteins about 3 orders of magnitude lower than limit of detection of the conventional ELISA approach.[26,25]

In conclusion, we have demonstrated a top-down approach for In_2O_3 nanoribbon FET fabrication using two photolithographic masks to define the position and the dimensions of the metal electrodes and the nanoribbons. Devices fabricated using this approach show good, uniform electrical performance without requiring doping or postprocess annealing. The fabrication is highly scalable, low cost, and a low temperature process that is compatible with the CMOS fabrication facilities. In_2O_3 is selected for the nanoribbon material because its electrical performance and long-term stability in aqueous solution are better than other metal oxide materials. In_2O_3 nanoribbon devices exhibited good sensitivity in both wide range of pH solution from pH 4 to 9 and physiological range between 6.7 and 8.2. Streptavidin−biotin has been chosen to demonstrate signal amplifying electronic ELISA with picomolar sensitivity showing 15% changes in normalized current. We demonstrated electronic ELISA for detection of HIV p24 proteins at concentration about 20 fg/mL or 250 viruses/mL, which is about 3 orders of magnitude lower than the commercial ELISA kit on the market. Depending on choice of capture probes, our uniform, scalable, sensitive, top-down In_2O_3 nanoribbon biosensor platform integrated with the electronic ELISA technique can be utilized for diagnosis of other infectious diseases and cancers. We believe that our In_2O_3 nanoribbon platform can be applied to other biological and medical applications.

■ ASSOCIATED CONTENT

Ⓢ Supporting Information

Materials and methods for device fabrication, surface functionalization, anchoring of amine probe molecules, synthesis of biotinylated linker molecules. Schematic diagram of synthesis of biotinylated linker molecules. In_2O_3 nanoribbon Debye length calculation. Fluorescent confirmation of phosphonic acid chemistry using biotin−streptavidin. Family plots of $I_{DS}-V_{DS}$ and $I_{DS}-V_{GS}$ of InGaZnO, SnO_2, and ITO nanoribbon ribbon devices. Optical images of a ZnO nanoribbon device before and after incubating in 1× PBS for 14 h. Distribution of electrical performance measured from 30 In_2O_3 nanoribbon devices in 0.01× PBS solution: I_{ON}, g_m, V_{TH}, and on/off current ratios. Plots of XRD results before and after annealing in low vacuum at 300 °C for 30 min. Comparison of average pH sensing responses between as-sputtered and annealed devices. Electrical parameters of In_2O_3 nanoribbon devices in 1× PBS during long-term stability test. Schematic diagrams for surface functionalization on samples and their negative controls for fluorescent experiments. Schematic diagram and an optical image of In_2O_3 pad on substrates used in the fluorescent experiment. Fluorescent images of samples and negative control of In_2O_3 pads on SiO_2 and Si_3N_4 substrates. A photograph and a fluorescent image of an In_2O_3 nanoribbon after incubating with 1 μM streptavidin with red dye. A real-time response of an In_2O_3 nanoribbon device exposed to 100 mM urea without presence of urease enzymes as a control experiment. Plots of $I_{DS}-V_{LG}$ measured from devices with and without In_2O_3 nanoribbon in 0.01× PBS. Plots of I_{DS} versus time measured from devices with and without In_2O_3 nanoribbon in 0.01× PBS. This material is available free of charge via the Internet at http://pubs.acs.org.

AUTHOR INFORMATION

Corresponding Authors

*E-mail: chongwuz@usc.edu
*E-mail: rdatar@med.miami.edu.

Author Contributions

[¶]The manuscript was written through contributions of all authors. All authors have given approval to the final version of the manuscript. These authors contributed equally.

Notes

The authors declare no competing financial interest.

ACKNOWLEDGMENTS

The authors acknowledge financial support from the L.K. Whittier Foundation, Ming Hsieh Institute, the National Institute of Health (NIBIB 5R01EB008275-04), Center for AIDS Research and Biomedical Nanotechnology Institute at the University of Miami (BioNIUM). We would like to thank Maoqing Yao for his help in device fabrication.

REFERENCES

(1) Cui, Y.; Wei, Q.; Park, H.; Lieber, C. M. *Science* **2001**, *293*, 1289−1292.

(2) Stern, E.; Klemic, J. F.; Routenberg, D. A.; Wyrembak, P. N.; Turner-Evans, D. B.; Hamilton, A. D.; LaVan, D. A.; Fahmy, T. M.; Reed, M. A. *Nature* **2007**, *445*, 519−522.

(3) Li, C.; Curreli, M.; Lin, H.; Lei, B.; Ishikawa, F. N.; Datar, R.; Cote, R. J.; Thompson, M. E.; Zhou, C. *J. Am. Chem. Soc.* **2005**, *127*, 12484−12485.

(4) Ishikawa, F. N.; Chang, H. K.; Curreli, M.; Liao, H. I.; Olson, C. A.; Chen, P. C.; Zhang, R.; Roberts, R. W.; Sun, R.; Cote, R. J.; Thompson, M. E.; Zhou, C. *ACS Nano* **2009**, *3*, 1219−1224.

(5) Chang, H. K.; Ishikawa, F. N.; Zhang, R.; Datar, R.; Cote, R. J.; Thompson, M. E.; Zhou, C. *ACS Nano* **2011**, *5*, 9883−9891.

(6) Hahm, J.; Lieber, C. M. *Nano Lett.* **2004**, *4*, 51−54.

(7) Gao, A.; Lu, N.; Dai, P.; Li, T.; Pei, H.; Gao, X.; Gong, Y.; Wang, Y.; Fan, C. *Nano Lett.* **2011**, *11*, 3974−3978.

(8) Patolsky, F.; Zheng, G. F.; Hayden, O.; Lakadamyali, M.; Zhuang, X. W.; Lieber, C. M. *P Natl. Acad. Sci. U.S.A.* **2004**, *101*, 14017−14022.

(9) Lin, C. H.; Hsiao, C. Y.; Hung, C. H.; Lo, Y. R.; Lee, C. C.; Su, C. J.; Lin, H. C.; Ko, F. H.; Huang, T. Y.; Yang, Y. S. *Chem. Commun. (Cambridge, U.K.)* **2008**, 5749−5751.

(10) Cui, Y.; Lauhon, L. J.; Gudiksen, M. S.; Wang, J. F.; Lieber, C. M. *Appl. Phys. Lett.* **2001**, *78*, 2214−2216.

(11) Elfström, N.; Karlström, A. E.; Linnros, J. *Nano Lett.* **2008**, *8*, 945−949.

(12) Hakim, M. M. A.; Lombardini, M.; Sun, K.; Giustiniano, F.; Roach, P. L.; Davies, D. E.; Howarth, P. H.; de Planque, M. R. R.; Morgan, H.; Ashburn, P. *Nano Lett.* **2012**, *12*, 1868−1872.

(13) Chang, H.-K.; Wang, X.; Aroonyadet, N.; Zhang, R.; Song, Y.; Datar, R.; Cote, R.; Thompson, M.; Zhou, C. *Mater. Res. Soc. Symp. Proc.* **2013**, 1569.

(14) Park, I.; Li, Z.; Pisano, A. P.; Williams, R. S. *Nanotechnology* **2010**, *21*, 015501.

(15) Wang, D.; Sheriff, B. A.; Heath, J. R. *Nano Lett.* **2006**, *6*, 1096−1100.

(16) Vacic, A.; Criscione, J. M.; Stern, E.; Rajan, N. K.; Fahmy, T.; Reed, M. A. *Biosens .Bioelectron.* **2011**, *28*, 239−242.

(17) Wang, X.; Aroonyadet, N.; Zhang, Y.; Mecklenburg, M.; Fang, X.; Chen, H.; Goo, E.; Zhou, C. *Nano Lett.* **2014**, *14*, 3014−3022.

(18) Zhang, D.; Liu, Z. Q.; Li, C.; Tang, T.; Liu, X. L.; Han, S.; Lei, B.; Zhou, C. W. *Nano Lett.* **2004**, *4*, 1919−1924.

(19) Chen, P. C.; Sukcharoenchoke, S.; Ryu, K.; de Arco, L. G.; Badmaev, A.; Wang, C.; Zhou, C. W. *Adv. Mater.* **2010**, *22*, 1900−1904.

(20) Li, C.; Zhang, D.; Han, S.; Liu, X.; Tang, T.; Lei, B.; Liu, Z.; Zhou, C. *Ann. N. Y. Acad. Sci.* **2003**, *1006*, 104−121.

(21) Zhang, D.; Li, C.; Han, S.; Liu, X.; Tang, T.; Jin, W.; Zhou, C. *Appl. Phys. A: Mater. Sci. Process.* **2003**, *77*, 163−166.

(22) Ju, S.; Facchetti, A.; Xuan, Y.; Liu, J.; Ishikawa, F.; Ye, P.; Zhou, C.; Marks, T. J.; Janes, D. B. *Nat. Nanotechnol.* **2007**, *2*, 378−384.

(23) Chen, P. C.; Shen, G. Z.; Chen, H. T.; Ha, Y. G.; Wu, C.; Sukcharoenchoke, S.; Fu, Y.; Liu, J.; Facchetti, A.; Marks, T. J.; Thompson, M. E.; Zhou, C. W. *ACS Nano* **2009**, *3*, 3383−3390.

(24) Fiebig, E. W.; Wright, D. J.; Rawal, B. D.; Garrett, P. E.; Schumacher, R. T.; Peddada, L.; Heldebrant, C.; Smith, R.; Conrad, A.; Kleinman, S. H.; Busch, M. P. *AIDS* **2003**, *17*, 1871−1879.

(25) Sutthent, R.; Gaudart, N.; Chokpaibulkit, K.; Tanliang, N.; Kanoksinsombath, C.; Chaisilwatana, P. *J. Clin. Microbiol.* **2003**, *41*, 1016−1022.

(26) Tang, S.; Hewlett, I. *J. Infect. Dis.* **2010**, *201* (Suppl 1), S59−64.

(27) Zheng, L.; Jia, L.; Li, B.; Situ, B.; Liu, Q.; Wang, Q.; Gan, N. *Molecules* **2012**, *17*, 5988−6000.

(28) Chang, L.; Song, L.; Fournier, D. R.; Kan, C. W.; Patel, P. P.; Ferrell, E. P.; Pink, B. A.; Minnehan, K. A.; Hanlon, D. W.; Duffy, D. C.; Wilson, D. H. *J. Virol. Methods* **2013**, *188*, 153−160.

(29) Lee, K.-B.; Kim, E.-Y.; Mirkin, C. A.; Wolinsky, S. M. *Nano Lett.* **2004**, *4*, 1869−1872.

(30) Rutstein, S. E.; Kamwendo, D.; Lugali, L.; Thengolose, I.; Tegha, G.; Fiscus, S. A.; Nelson, J. A. E.; Hosseinipour, M. C.; Sarr, A.; Gupta, S.; Chimbwandira, F.; Mwenda, R.; Mataya, R. *J. Clin. Virol.* **2014**, *60*, 392−398.

(31) Schockmel, G. A.; Yerly, S.; Perrin, L. *J. Acquired Immune Defic. Syndr.* **1997**, *14*, 179−183.

(32) Zhou, W.; Dai, X. C.; Fu, T. M.; Xie, C.; Liu, J.; Lieber, C. M. *Nano Lett.* **2014**, *14*, 1614−1619.

(33) Bellingham, J. R.; Phillips, W. A.; Adkins, C. J. *J. Phys.: Condens. Matter* **1990**, *2*, 6207−6221.

(34) Yuan, Z. J.; Zhu, X. M.; Wang, X. O.; Cai, X. K.; Zhang, B. P.; Qiu, D. J.; Wu, H. Z. *Thin Solid Films* **2011**, *519*, 3254−3258.

(35) Butler, J. E. *J. Immunoassay* **2000**, *21*, 165−209.

(36) Stern, E.; Vacic, A.; Li, C.; Ishikawa, F. N.; Zhou, C.; Reed, M. A.; Fahmy, T. M. *Small* **2010**, *6*, 232−238.

(37) Krebs, H. A. *Annu. Rev. Biochem.* **1950**, *19*, 409−430.